

Design Considerations for Micro-Glassblown Atomic Vapor Cells

Radwan M. Noor¹, *Student Member, IEEE*, Mohammad H. Asadian², *Student Member, IEEE*,
and Andrei M. Shkel³, *Fellow, IEEE*

Abstract—This paper presents a design process for miniaturized atomic vapor cells using the micro-glassblowing process. It discusses multiple design considerations, including cell geometry, optical properties, materials, and surface coating. The geometry and the optical properties were studied using experimentally verified analytical and Finite Element Models (FEM). The cell construction material and surface coating were the focus of our experimental study on factors that affect the relaxation time (T₂) of nuclear spins. We showed that the wafer-level coating process with Al₂O₃ increased the ¹³¹Xe T₂ by 3× and by switching from Borosilicate glass (Pyrex) to Aluminosilicate glass (ASG), T₂ was improved by 2.5×, for the same species. The improvement in the T₂ is projected to reduce the ARW of an NMR gyro and the sensitivity of an NMR magnetometer by 3× with Al₂O₃ coated cells and by 2.5× with ASG cells. [2019-0158]

Index Terms—Glassblowing, atomic sensors, microfabrication, nuclear magnetic resonance (NMR), NMR gyroscopes, atomic cells, relaxation time.

I. INTRODUCTION

MINIATURIZATION of atomic vapor cells is a critical technology for chip-scale “hot” and “cold” atomic-microsystems. These microsystems include, but are not limited to, chip-scale magnetometers [2]–[4], clocks [5], and gyroscopes [4], [6], [7].

Some of the challenges in cells development that arise from miniaturization include development of: a batch fabrication process that yields small size, weight, power, and cost (SWAP+C) cells [8]; low SWAP+C cells with geometrical

requirements such as multiple optical ports and cell symmetry; cells with homogeneous wall material; wall coatings and materials that preserve the atomic polarization inside the cells.

Multiport cells are needed for applications such as Nuclear Magnetic Resonance (NMR) gyros and magnetometers, [9], [10], while symmetry is preferred for all atomic vapor cells to avoid unwanted phenomena, such as self-magnetization and quadrupole shift, [11]. In-homogeneity in the cell wall material increases cell asymmetry, [12], which increases quadrupole frequency shift that negatively affects the performance of NMR atomic sensors. Additionally, with miniaturization of atomic cells, the interaction of atomic vapor with the cell walls increases due to the increase of the surface area to volume ratio, [13]. This calls for a careful selection of cell materials and surface treatment processes.

The fabrication and filling of miniaturized-glassblown spherical cells, [1], [14]–[16], enabled a wafer-level fabrication of highly spherical axisymmetric multiport cells with homogeneous wall material that addressed some of cell design challenges. In this paper, we discuss design process considerations, which were not previously considered, including geometry, optical properties, materials, and surface treatment (coating). The design process combines analytical, [14], and finite element modeling (FEM) of the cell’s geometry and optical properties, [17], [18], that are backed up by experimental validation. In this paper, we also expand on our study of cell wall materials and surface coating.

This paper is structured as follows. In Section II, we briefly described the overall design approach of miniaturized cells. Then, in Section III, we discuss the geometrical aspect of the cell fabrication, where we introduced analytical and finite element models and, subsequently, supported results of analysis by experimental validation. In Section IV, we presented the optical modeling and simulation results of the fabricated cells backed up by experimental validation. Section V talks about a study of materials and cell wall coating on the performance of atomic cells. Section VI concludes the paper with an outlook on the spectrum of applications that can benefit from the presented design approach.

II. GLASSBLOWING PROCESS

Glassblowing of miniaturized cells on a wafer-level is based on anodic bonding a glass wafer to a silicon wafer with pre-etched cavities under atmospheric pressure conditions.

Manuscript received July 9, 2019; revised September 16, 2019; accepted October 6, 2019. This work was supported by Agency for Defense Development (ADD) under Award ADD-208376. The work of R. M. Noor was supported by the King Abdulaziz City for Science and Technology (KACST). Subject Editor C. Nguyen. (*Corresponding author: Radwan M. Noor.*)

R. M. Noor is with the Microsystems Laboratory, Department of Electrical Engineering and Computer Science, University of California, Irvine, CA 92697 USA, and with the National Center for MEMS Technology, King Abdulaziz City for Science and Technology (KACST), Riyadh 12354, Saudi Arabia (e-mail: rmmohamm@uci.edu).

M. H. Asadian is with the Microsystems Laboratory, Department of Mechanical and Aerospace Engineering, University of California, Irvine, CA 92697 USA (e-mail: asadianm@uci.edu).

A. M. Shkel is with the Department of Mechanical and Aerospace Engineering, University of California, Irvine, CA 92697 USA, with the Department of Electrical Engineering and Computer Sciences, University of California, Irvine, CA 92697 USA, and also with the Microsystems Laboratory, Department of Biomedical Engineering, University of California, Irvine, CA 92697 USA (e-mail: ashkel@uci.edu).

Color versions of one or more of the figures in this article are available online at <http://ieeexplore.ieee.org>.

Digital Object Identifier 10.1109/JMEMS.2019.2949084

The wafer stack is then heated up to a temperature higher than the softening point of the glass; the combination of glass softening and pressure build-up in the pre-etched cavities creates axisymmetric spherical shells, Fig. 1, [14].

After the glassblowing step, the cells are rapidly cooled down to preserve their shape and to prevent any crystallization of the glass, [19]. This rapid cooling puts a thermal shock on the cell walls and builds up stresses across the geometry. Additionally, the cooling process results in a pressure drop inside the cells, which creates a pressure difference across the cell walls. Depending on the pressure difference and wall thickness, breakage might happen at the thinnest part of the cell.

For analysis, we use a multi-step approach for designing miniaturized glassblown cells. The design process starts with an analytical model presented in [14], which estimates dimensions of the resulting geometry of cells. Next, a finite element model predicts a more realistic geometry of the cell using isothermal flow simulation in COMSOL. The resulting geometry is then exported to solid mechanics simulation, which estimates the maximum stress on the cell walls and predicts whether the cell can survive the force generated by the pressure difference across its walls. Finally, the model is exported to optical simulation software to simulate the optical behavior of the cells.

III. GEOMETRY

In this section, we present an analytical model and FEM model, and in light of the two models, we discuss the parameters that influence the geometry of the cells, such as their size, sphericity, and wall thickness. Subsequently, we present experimental characterization that validates the simulation results.

A. Analytical Model

The height h_g and the inner radius of the cell r_g , shown in Fig. 1, are given by equations (1) and (2), respectively, [14]

$$h_g = \frac{\left[\left(3V_g + \sqrt{r_o^6 \pi^2 + 9V_g^2} \right) \pi^2 \right]^{2/3} - r_o^2 \pi^2}{\pi \left[\left(3V_g + \sqrt{r_o^6 \pi^2 + 9V_g^2} \right) \pi^2 \right]^{1/3}} \quad (1)$$

$$r_g = \frac{h_g^2 + r_o^2}{2h_g}, \quad (2)$$

where V_g is the inner volume of the cell and is defined as

$$V_g = h_e \pi r_o^2 \left(\frac{T_f P_s}{T_s P_f} - 1 \right), \quad (3)$$

where T_f and T_s are temperatures of the glassblowing furnace and the cavity sealing measured in Kelvins, P_f and P_s are the pressure values (in Torr, for example) during the glassblowing and the cavity sealing, respectively, r_o is the radius of the etched cavity and h_e is the etched cavity depth. The average thickness of the cell wall can be estimated as [14],

$$\delta = \frac{\delta_0 r_o^2}{h_g^2 + r_o^2}, \quad (4)$$

where δ_0 is the initial glass layer thickness, as shown in Fig. 1.

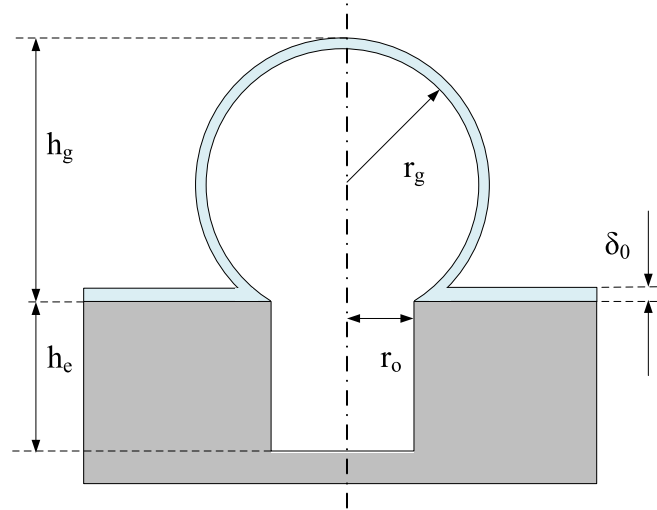


Fig. 1. Sketch of a cross sectional view of a glassblown cell.

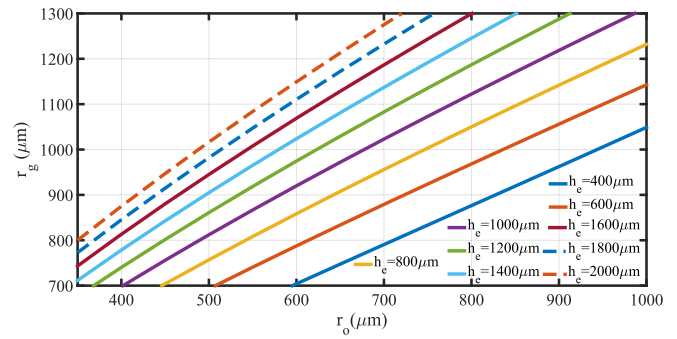


Fig. 2. Radius of glassblown cell r_g vs. the cavity radius r_o for different cavity depths h_e , ranging from $600\mu\text{m}$ to $2000\mu\text{m}$.

The glassblowing process parameters (r_o and h_e) can produce a wide variety of cell sizes and sphericity levels. Fig. 2 depicts a selected subset of these parameters. In this paper, our target application for the glassblown shells is miniaturized atomic cells, so a cell radius, r_g , on the order of 1mm is desired. A range of the cavity radii r_o , that produces a cell with $r_g = 1\text{mm}$, is from $488\mu\text{m}$ to $945\mu\text{m}$. However, as it was noted in [14], a smaller r_o is recommended to achieve higher sphericity cells.

The increase in cell sphericity reduces its asymmetry. Cells with high asymmetry have shown larger quadrupole splitting in ^{131}Xe frequency, [11].

B. Sphericity

The cell sphericity is defined as the ratio of the effective volume to the surface area of the exposed part of the cell above the glass wafer surface level, [20]. It is calculated as

$$\Psi = \frac{\pi^{1/3} (6V'_g)^{2/3}}{A_g}, \quad (5)$$

where V'_g and A_g are the volume and the surface area of the exposed part of the cell, which is above the glass wafer surface

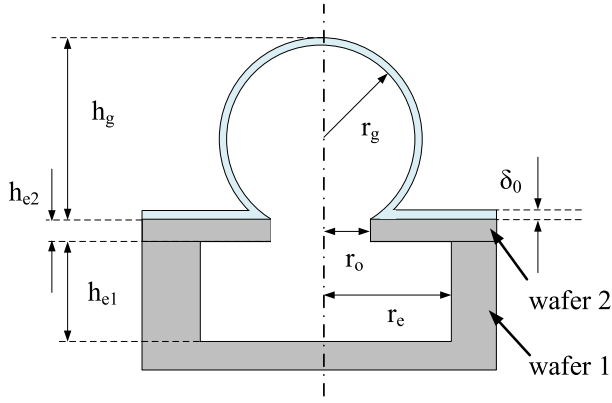


Fig. 3. Sketch of a cross sectional view of a glassblown cell using a dual-wafer approach to build the Si cavity.

level, and both are calculated as

$$V'_g = \frac{\pi}{3} h_{g|exp}^2 (3r_g - h_{g|exp}), \quad (6)$$

$$A_g = \pi h_{g|exp} (4r_g - h_{g|exp}), \quad (7)$$

where $h_{g|exp}$ is the height of the exposed part of the shell, defined as

$$h_{g|exp} = h_g - \delta_0 \quad (8)$$

Note, h_g is defined from the silicon /glass interface to the top of the cell, as shown in Fig. 1.

There are several approaches to produce cells with higher sphericity. These include controlling the process pressure, either by increasing the initial cavity pressure (P_s), [21], or reducing the glassblowing furnace pressure (P_f), [18], or both. Another approach is to increase the initial volume of the cavity while keeping the cavity radius r_o small, as it was suggested in [14]. In this process, a stack of two wafers was used to build the Si cavity. The first one is a thick Si wafer, 1mm for example, where large cavities are etched. The second wafer is a thin wafer, 100 μ m for example, bonded to the first wafer and smaller openings are etched through, Fig. 3. This approach allows for larger volume without sacrificing sphericity and relaxes the requirement on the depth of etching. The inner volume of the cell becomes

$$V_g = [h_{e1}\pi r_e^2 + h_{e2}\pi r_o^2] \left(\frac{T_f P_s}{T_s P_f} - 1 \right), \quad (9)$$

where h_{e1} and r_e are the cavity depth and radius of the wafer 1, and h_{e2} is the wafer 2 thickness.

To improve sphericity, one can reduce the glass thickness to increase the exposed part on top of the glass surface. However, that would create thin shells, and the pressure difference across the shell walls will create compressive stress that is larger than the compressive strength of the glass material, which would lead to breaking of the cell. To estimate the maximum cell volume, we created a finite element model, which is discussed next.

C. Finite Element Model

The glass wall thickness is not uniform in this process, [14], and since this parameter is essential to accurately predict the

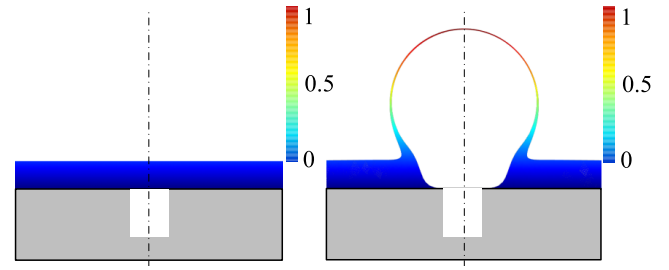


Fig. 4. FEM Simulation shows a cross sectional view of the sample before and after glassblowing. The scale bar represents the normalized displacement of glass during the glassblowing process.

light interaction with the cell walls, we used a finite element model using COMSOL Fluid Flow physics to estimate the wall thickness distribution in addition to the maximum volume of the cells. The developed model was adopted from our previous work, [17]. The shape of the glassblown cell at different time steps is predicted with a Newtonian isothermal fluid flow model with an adaptive re-meshing in COMSOL Multiphysics FE Package. In this model, the instantaneous volume and pressure of the cell and the cavity were calculated at each time step of the simulation, and once the equilibrium-state is reached the deformation of the glass layer stops. Fig. 4 shows snapshots of initial and final geometry of cell's cross-section during the glassblowing.

The resulting geometry from the fluid flow model was exported to a solid mechanics simulation, and the pressure difference after cooling was calculated and applied to the cell's outer surface to estimate the maximum stress value and location. The model predicted that the maximum stress was always concentrated at the top part of the cell and that it is because the shell's minimum thickness is at the top, which matches what was experimentally demonstrated earlier in [14].

D. Glass Thickness δ_0

Using a combination of the FEM model and compressive strength of the Borosilicate glass (100 MPa), we estimated the maximum cell volume that would survive the glassblowing process. This process was repeated for different ratios of the glass thickness δ_0 to the cavity opening r_o . Sphericity of the exposed part of the cell was calculated using equation (5). The trend in Fig. 5 shows that as we increase the glass thickness relative to the cavity radius, sphericity of the maximum cell size drops following closely a quadratic line equation

$$f(x) = ax^2 + bx + c, \quad (10)$$

where, x represents a normalized glass thickness (δ_0/r_o), and coefficients a , b and c are -2.55 ± 2.14 , -1.83 ± 5 , and 98.53 ± 2.57 , respectively, with 95% confidence bounds. Additionally, increasing the normalized glass thickness increases the thickness variation of the cell walls from top to bottom. On the other hand, the normalized radius (normalized radius is the radius of a three-point circle fitted to the top and two sides of the exposed part of the cell divided by the cavity opening r_o) of the maximum cell volume, that would survive

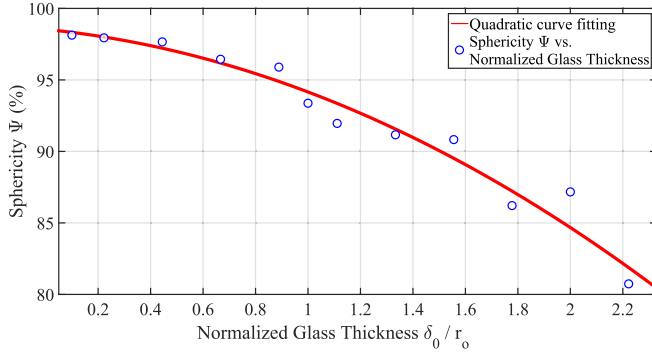


Fig. 5. Sphericity of the maximum cell volume vs. the normalized glass thickness estimated using FEM modeling. Normalized glass thickness is the ratio of the glass thickness δ_0 to the cavity radius r_0 .

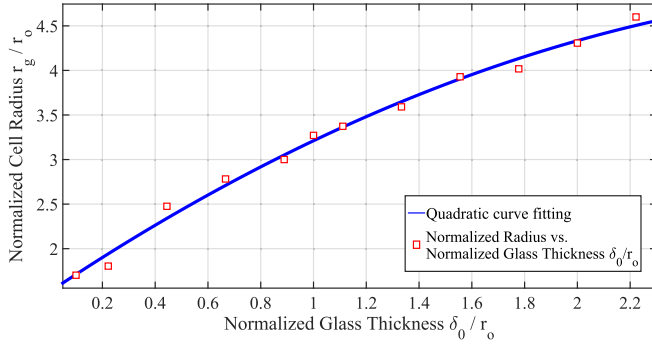


Fig. 6. Normalized radius of the maximum cell volume (r_g/r_0) vs. normalized glass thickness (δ_0/r_0), estimated using FEM modeling.

the glassblowing and the subsequent cooling, was found to increase quadratically with the increase of the glass thickness relative to the cavity radius r_0 . The equation parameters of the curve fitting line in Fig. 6, a , b and c are -0.29 ± 0.16 , 1.98 ± 0.4 , and 1.516 ± 0.2 , respectively, with 95% confidence bounds.

From Fig. 5 we deduce that in order to achieve a high sphericity level, one should use a glass thickness, that is $1/10^{th}$ of the cavity radius r_0 . From Fig. 6, r_0 should be on the order of $1.7 \times$ of the desired cell radius r_g . For example, if a cell of radius 1mm is desired, the cavity opening radius r_0 should be $588 \mu\text{m}$ and the glass thickness δ_0 should be $\approx 59 \mu\text{m}$, to achieve $\approx 98\%$ sphericity. From equation (4), the average thickness of the resulting shell will be $\approx 6.5 \mu\text{m}$. While this combination of parameters would survive the pressure difference due to glassblowing, from a practical point of view, it might not survive other steps of the process, such as backside opening and subsequent wet cleaning.

E. Characterization of Geometry

To validate the model, we fabricated two samples on a 1mm thick wafer, and 350 μm glass (Pyrex) thickness, the Si cavity radii for the samples were 225 μm and 300 μm , while the etch depth was 700 μm . The measured cell radius and height of these cells are presented in Table I. Visual inspection shows that an agreement between the fabricated cell and the geometry

TABLE I
COMPARISON BETWEEN SIMULATED AND EXPERIMENTALLY
MEASURED PARAMETERS OF TWO FABRICATED SAMPLES,
(ALL MEASUREMENTS ARE IN (mm))

	Simulation		Experiment	
	Radius	Height	Radius	Height
Cell 1	0.78	1.33	0.79	1.34
Cell 2	0.93	1.67	0.98	1.71

predicted by the FEM simulation, in terms of the cell height and radius, is within 95%.

IV. OPTICAL PROPERTIES

In this section, we present an optical simulation model and discuss optical properties of the glassblown cells. The optical properties of interest for the atomic cells are light transmission through the cell and variation in optical polarization. Both parameters are critical for designs of NMR sensors.

A. Simulation

The optical simulation was performed using Monte Carlo ray tracing method, [22]. In this method, the light beam is broken down to a large number of individual rays and the interaction of those rays with different parts of the miniaturized cell is then integrated using Monte Carlo integration to predict the behavior of the whole beam within the cell.

The simulation shows that due to the change of the cell wall thickness, different parts of the beam experience different diffraction angles. The bottom part of the cell is usually the thickest, which causes the beam at that section to diffract downward and be trapped in the cell, bundle “A” in Fig. 7-(top). The mid-section of the beam transmits through the cell; however, it still experiences downward bending, as it propagates out of the cell, bundle “B” in Fig. 7-(top). Additionally, the beam polarization was analyzed by grouping individual rays into pockets and averaging their polarization parameters (ellipticity and azimuth angle). The polarization maps in Fig. 8 show that the cell preserves the azimuth angle and ellipticity for the majority of the transmitted beam, Fig. 8-a) and Fig. 8-b), respectively, and the degree of polarization is within 95%. This polarization distortion is negligible and it does not affect the operation of sensors.

The simulation also shows that cells with small normalized glass thickness and high sphericity pass the light beam through with minimal diffraction, Fig. 7-(bottom).

B. Optical Characterization

We measured the optical properties of the fabricated samples, discussed in Section III-E. The experimental setup consisted of a laser beam, a linear polarizer, and a quarter wave plate, creating a circularly polarized light that enters the sample. The transmitted light then propagates to a polarimeter (Thorlabs PAX 5710). The power and polarization of the optical beam were measured before and after the transmission through the samples. The beam radius was $\approx 0.5 \times$ of the cell

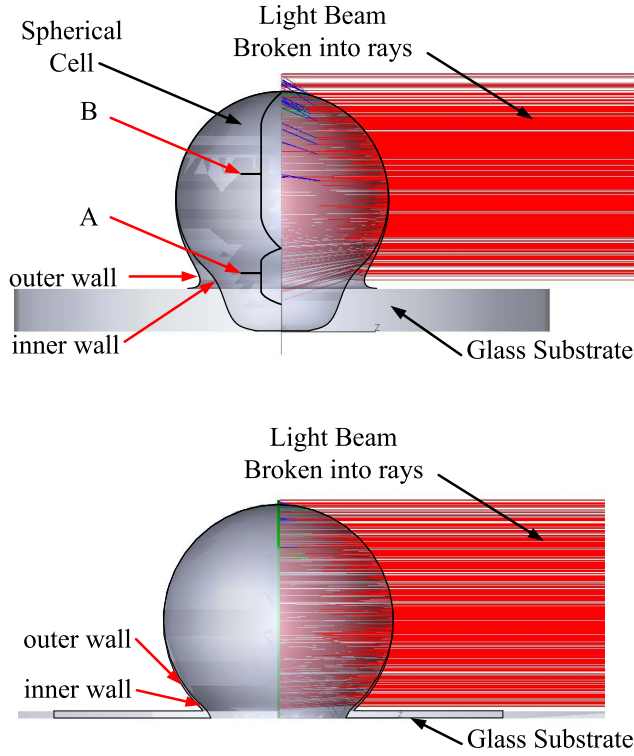


Fig. 7. Cross-section illustration showing the interaction of the optical beam with the cell. Top: 89% sphericity, Bottom: 98% sphericity. Ray bundle (A) in the top illustration experience the most diffraction and are trapped into the cell.

TABLE II
COMPARISON OF OPTICAL PROPERTIES OF TWO CELLS

	Power Transmission		Polarization (ellipticity)	
	Simulation	Experiment	Simulation	Experiment
Cell 1	86.2%	80.6%	1.43°	1.3°
Cell 2	86.2%	83.1%	1.55°	3.8°

radius. Table II shows a comparison between the measured and simulated optical transmission and polarization of the two fabricated samples. The simulation results are consistent with the well-known 4% per surface loss at an air/glass interface. The discrepancy between the measured and simulated values can be a result of the parasitic glass bubbles on the samples due to defects that could have blocked a part of the transmitted light and changed its polarization.

As mentioned earlier, micro-glassblown cells have multiple in-plane and out-of-plane ports. Even though in-plane ports provide optical paths for light transmission through the cell, the cells are not perfectly symmetric around them, and the beam would experience a downward bending, as discussed earlier. On the other hand, the cells are axisymmetric around the out-of-plane port, but their transmission is limited by the glassblowing cavity opening r_o , which is on the order of $1/2$ of the cell radius r_g . To estimate the optimal orientation of light coupling to atomic sensors, we used the optical magnetometer scale factor as a metric to compare different orientations. The first configuration is in-plane (horizontal) pumping and probing, Fig. 9-(a); the second configuration is out-of-plane (vertical) pumping and horizontal probing, 9-b).

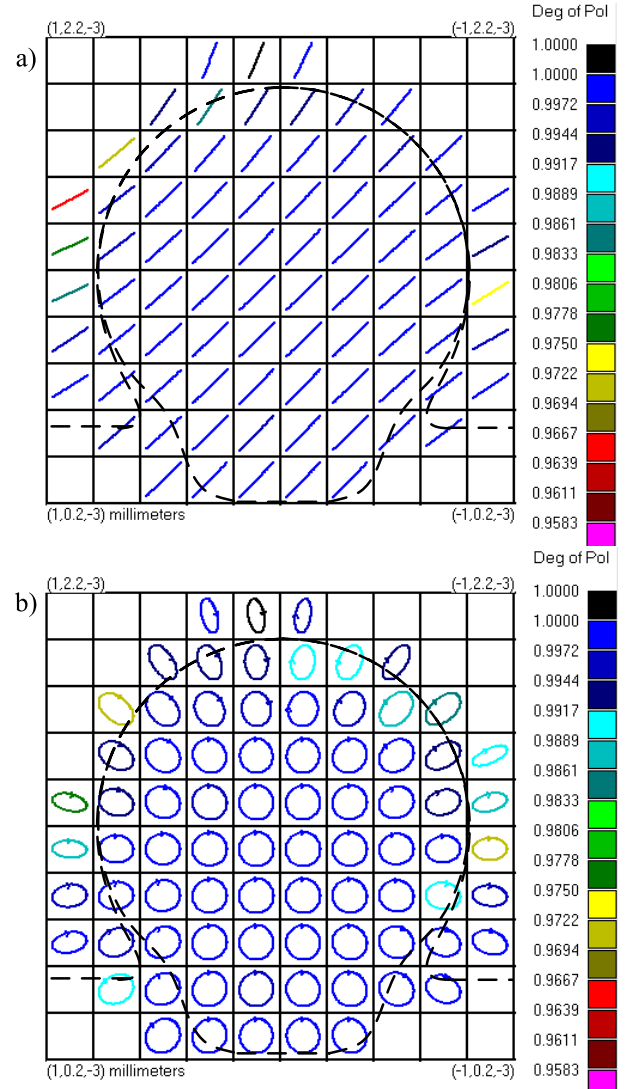


Fig. 8. Simulation results of the transmitted beam polarization for two cases: a) +45 linearly polarized light, b) right circular polarized light. Dashed lines represent the outer borders of the cell. Only the beam pockets on edges of the cell experience polarization changes, either in the polarization angle or ellipticity, while the majority of the beam's polarization is unchanged.

Fig. 10 shows the Rubidium magnetometer response of the two configurations; the vertical pumping improved the magnetometer scale factor by $2\times$.

V. FILLING AND COATING

In this section, the filling and coating process of miniaturized spherical atomic cells are discussed. We briefly introduce the fabrication and filling process followed by a study on different wall materials and coating and experimentally measured their effect on the nuclear spins relaxation.

A. Background

The transverse relaxation time of the noble gas atoms is directly related to the performance of NMR sensors. For gyroscopes, for example, the angle random walk (ARW) is

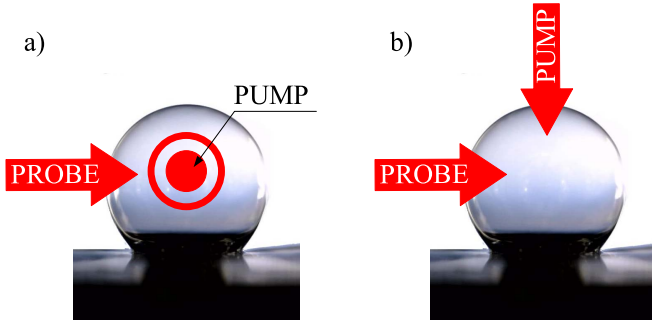


Fig. 9. Illustration of two different orientations of pumping and probing: (a) in plane pumping and probing, (b) out-of-plane pumping and in-plane probing.

predicted to depend on T_2 time as follows, [23],

$$ARW = \frac{3600}{T_2 \times SNR \sqrt{\delta f}} [^\circ / \sqrt{hr}], \quad (11)$$

where T_2 is the transverse relaxation time of the Xe atoms, SNR is the signal-to-noise ratio of the electron paramagnetic resonance (EPR) magnetometer, and δf is bandwidth of the phase noise in Hz. The fundamental sensitivity limit of an NMR magnetometer (NMRM) depends on the T_2 time as, [10],

$$\delta B_n = \frac{1}{2\pi \gamma T_2} \times \frac{\delta B_e}{P \times dB_n/dP}, \quad (12)$$

where δB_e is the noise floor of the EPR magnetometer, P is the percentage of polarized Xe atoms, dB_n/dP is the magnetic field produced by Xe atoms per unit polarization, taking into consideration the “enhancement factor” of direct interaction with the alkali metal vapor, [24]. Several factors can affect the relaxation time of the noble gas atoms in atomic vapor cells, summarized as, [25], [26],

$$\frac{1}{T_{2|total}} = \frac{1}{T_{2|coll}} + \frac{1}{T_2'} + \frac{1}{T_{2|\Delta B}} + \frac{1}{T_{2|wall}}, \quad (13)$$

where, $T_{2|total}$ is the effective transverse relaxation time, $T_{2|coll}$ is the relaxation time due to collisions with alkali metal atoms, T_2' is the relaxation time due to self-collision of Xe atoms, $T_{2|\Delta B}$ is the relaxation time due to magnetic field inhomogeneity inside the cell, and $T_{2|wall}$ is the relaxation time due to collisions of atoms with cell walls. In mm-sized cells, the wall collisions and spin exchange relaxation are dominant, [13], and therefore special care needs to be taken during the cell construction.

B. Fabrication and Filling Process

There are multiple filling approaches to introduce alkali metal and buffer gas in the miniaturized cells. The approaches have been discussed widely throughout the literature, [27]–[34]. The approach that we adopted in this paper for filling cells using an on-chip alkali metal dispenser was introduced previously for planar cells in [35] and [36]. A recent study that reviewed those approaches for atomic clocks, [37], comes to the conclusion that a filling process like the one suggested here, which combines an on-chip dispensing alkali source with high-temperature anodic bonding, has excellent

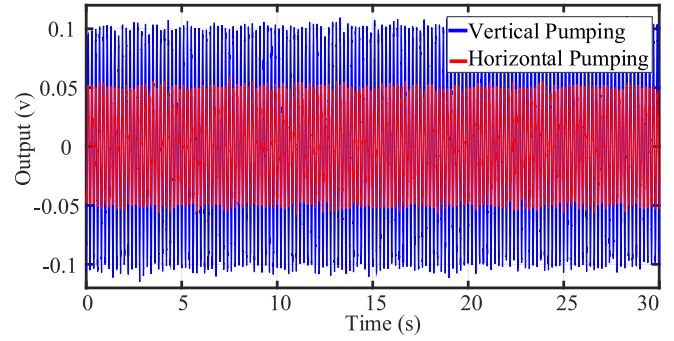


Fig. 10. Experimental results of Rb magnetometer signals for vertical (blue) and horizontal (red) pumping. The figure shows that vertical pump improved the Rb magnetometer scale factor by 2 \times .

MEMS compatibility, internal atmosphere quality, and process repeatability.

The fabrication process starts by etching 700 μm cavities in a 1 mm thick Si wafer, Fig. 11-(a). Next, the first anodic bonding seals the etched cavities under atmospheric pressure, Fig. 11-(b). After placing the wafer stack in a high-temperature furnace at 850 $^\circ\text{C}$ for Borosilicate glass (Pyrex) and 1000 $^\circ\text{C}$ for Aluminosilicate glass (ASG) for 5-7 minutes, spherically shaped glass shells are formed, [14], Fig. 11-(c). The formation was due to two effects: the trapped air inside the cavities builds up the pressure due to the temperature increase, and the glass transitions from a solid state to a viscous state.

The next steps in the process are to open the backside of Si wafer and to define 100 μm deep micro-channels using Deep Reactive Ion Etching (DRIE), Fig. 11-(d). Subsequently, the cell coating was applied via atomic layer deposition (ALD) of 10 nm aluminum oxide (Al_2O_3) to the opened cells and the capping wafer, Fig. 11-(e).

The second anodic bonding took place after the alkali dispenser pills have been placed in the central cell, with the ALD Al_2O_3 as an intermediate layer between the backside of the Si wafer and the capping glass wafer, Fig. 11-(f). The wafer alignment for bonding was performed inside a chamber with a noble gas and a buffer gas at pressures of 250-350 Torr, Fig. 11-(f). After the bonding process was complete, each dispenser was activated by focusing a 3.5-4W laser for 15 seconds, which released the alkali vapor to satellite cells, Fig. 11-(g).

C. Design of Experiment

The study aims to test the effects of different materials and surface coatings on relaxation time of Xe atoms by isolating all factors that affect the relaxation, except for the effect of wall interactions. Three samples were fabricated. The first (PXE01) was fabricated using Borosilicate glass (Pyrex) and was utilized as a baseline in our study; the second (PAXE01) was made with Pyrex and coated using Atomic Layer Deposition (ALD) of 10nm Aluminum Oxide (Al_2O_3); the third (HXE02) was fabricated using Aluminosilicate glass (ASG). To isolate other factors beside cell walls, the samples were filled with similar amounts of noble and buffer gases, and were tested under the same conditions of temperature and

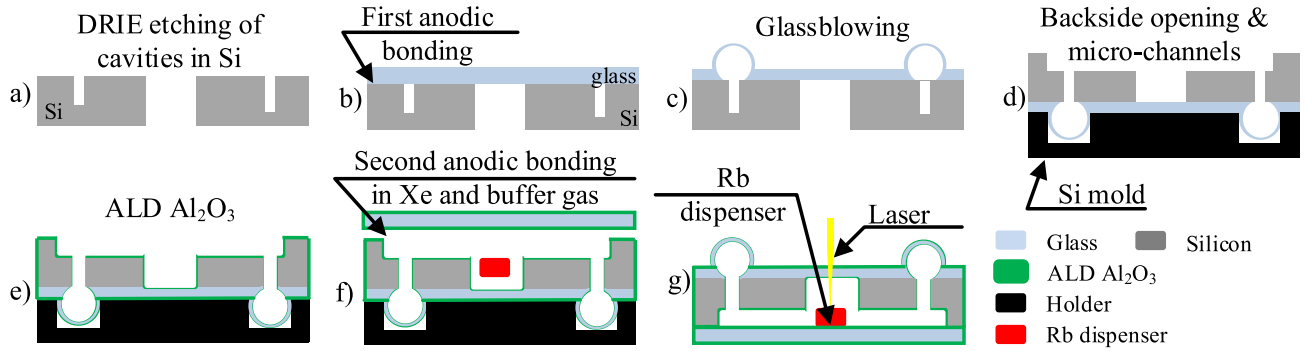


Fig. 11. Description of the process flow: (a) DRIE etching of 700 μ m and through wafer cavities in 1mm Si wafer, (b) first anodic bonding of glass to the etched Si wafer, (c) glassblowing of cells, (d) cell back-side opening and channel definition using DRIE etching, (e) Atomic Layer Deposition (ALD) of 10nm Al₂O₃, (f) loading the Rb dispenser and performing the second anodic bonding in a noble gas and buffer gas filled chamber, (g) dispensing alkali metal through micro channels by laser heating of Rb source.

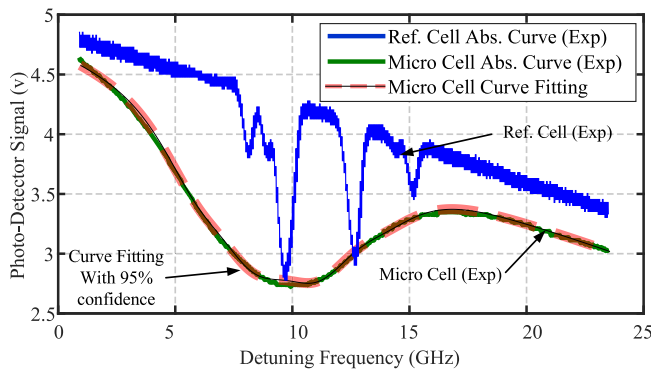


Fig. 12. Measured Rb absorption curve for the reference cell (blue) shows multiple distinguishable absorption peaks. Measured absorption of a micro cell (green), the cell was filled with 300 Torr of only N₂ and Rb, which broadened and shifted the peaks. In curve fitting to the micro cell spectrum (dashed red), the width of the curve represents 95% confidence bounds, which confirmed a close fit to the experimentally measured data.

magnetic field levels. Optical heating was used to minimize any interference from resistive heaters.

The pressure values at room temperature were: 65 Torr, 45 Torr and 300 Torr for natural Xe, Ne, and N₂, respectively. A data fitting of the Rb absorption curve (obtained by sweeping the wavelength of the VCSEL beam passing through the cell) was used to confirm the amount of noble and buffer gasses inside the cell. Measurements showed a reduction of the N₂ gas pressure by 20%-30%, which was attributed to absorption by the getter material in the Rb pill. The experimentally measured relaxation time (T_2) of ¹²⁹Xe and ¹³¹Xe isotopes were used to compare cells. The cells were heated optically using a 2.5W laser source at 1550nm, focusing only on the Si part of the cell substrate. We used the free induction decay (FID) method to estimate the relaxation rate using a dual beam scheme, one for pumping and another for detection, Fig. 13. The FID experiment was performed by applying a static magnetic field B_0 along the pump axis, the z-axis in this case, which will cause the nuclear spins to precesses at their Larmor frequency ω_L about the z-axis, then applying a $\pi/2$ pulse with a frequency ω_a equal to the ω_L of the isotope of interest on a perpendicular axis to

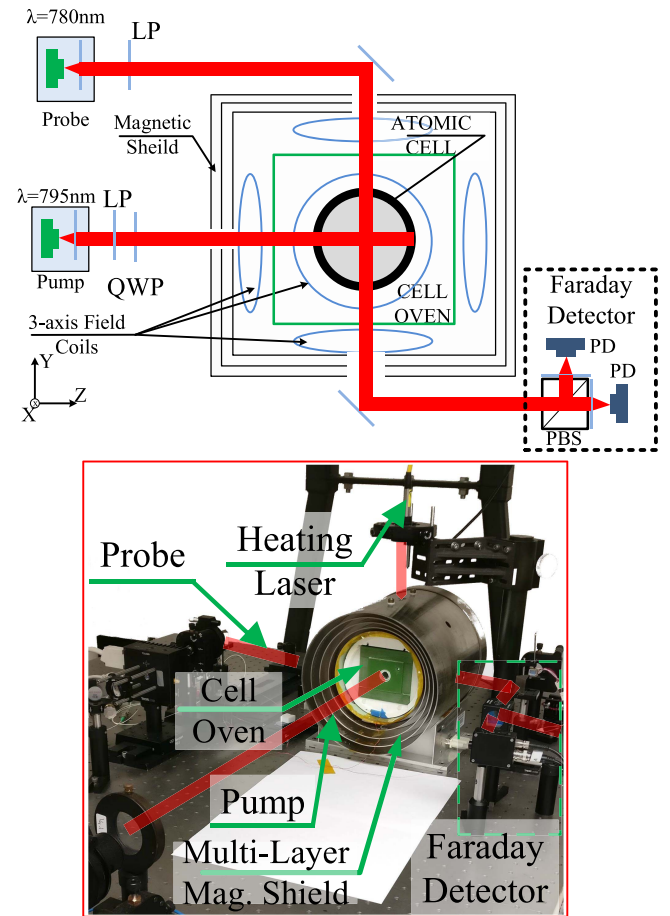


Fig. 13. Top: Dual beam optical setup for characterization of cells. (LP: linear polarizer, QWP: quarter wave plate, PBS: polarizing beam splitter, PD: photo detector, Faraday Detector: a balanced polarimeter used to detect Faraday rotation). Bottom: Picture of the experimental setup showing the pump, probe, and the heating laser beams, as well as the nested magnetic shields and the cell oven.

the pump axis, the y-axis here. The pulse would abruptly deflect the magnetization vector of the nuclear spins to the xy-plane. A signal proportional to the nuclear spins as they re-align to the pump axis is detected along the y-axis, and an exponentially decaying sinusoidal wave was measured at a frequency equal to the Larmor frequency ω_L and a decay

constant proportional to the transverse relaxation time T_2 of the isotope of interest. The detection was carried out by the probe beam which detected precession of the Rb about the effective field caused by the Xe and the applied field.

D. Gas Content Measurement

Buffer and noble gasses contribute to the Rb transition line by broadening the light absorption spectrum and shifting the frequency of absorption by specific values for each gas, reported in [38] and [39]. The absorption data were fitted to a Voigt profile, which is a convolution between a Gaussian and Lorentzian functions, [40]. The Gaussian function accounts for Doppler broadening, while the Lorentzian function estimates broadening due to collisions with the buffer gas. An approximated Voigt profile is defined as, [40],

$$F(x) = ax + b - \sum_{i=1}^8 \left[\eta / \left(1 + \left(\frac{x - x_i}{0.5\Gamma_i} \right)^2 \right) + (1 - \eta) \exp \left(-\frac{(x - x_i)^2}{c\Gamma_i} \right) \right], \quad (14)$$

where a and b are parameters of a line, $c = 1/(2\sqrt{\ln 2})$, and η is the Lorentzian constant and its value is between 0 and 1. For each of the four ground transitions of ^{85}Rb and ^{87}Rb , x_i is the center frequency of that transition in MHz, Γ_i is the Voigt width of that peak in MHz. The Voigt width is related to the Gaussian and the Lorentzian widths as follows, [41],

$$\Gamma_V = 0.5346 \Gamma_L + \sqrt{0.2166 \Gamma_L^2 + \Gamma_G^2}, \quad (15)$$

where Γ_V , Γ_L , Γ_G are the Voigt, the Lorentzian, and the Gaussian widths, respectively.

The Rb dispenser that was used in our process consisted of a pure alkali metal and a getter material (SAES St 101). Once the dispenser is activated, the alkali metal is released, and the getter material absorbs active gasses, such as O_2 , H_2 , CO , and N_2 . To estimate the amount of remaining N_2 gas, we filled an additional cell with 300 Torr of only N_2 gas. We split a laser beam in half and passed the two beams, one through a reference cell with only natural Rb and the other through our fabricated cell, with Rb and other gasses. By sweeping the laser wavelength, we obtained two Rb light absorption spectrum curves, one for the reference cell, where the ground transitions of each isotope ^{85}Rb and ^{87}Rb can be distinguished, the other is for the fabricated cell, where these transitions are broadened and shifted due to the N_2 gas, [38], [39]. Starting with the Rb light absorption spectrum of the reference cell and substituting for the broadening and frequency shift rates of N_2 in an iterative curve fitting, we were able to find the N_2 pressure that matched Rb light absorption spectrum curve of the fabricated sample. Fig. 12 shows the experimentally obtained Rb absorption curves for the reference cell, microcell with only Rb and N_2 , and the curve fit that satisfies the estimated N_2 gas pressure inside the cell. We measured the N_2 gas after two weeks of activation and found that the getter material in the Rb pill was saturated after absorbing 20% of the N_2 gas, [42]. Note that this particular getter absorbs gasses at different rates. The relative sorption rates of H_2 , O_2 ,

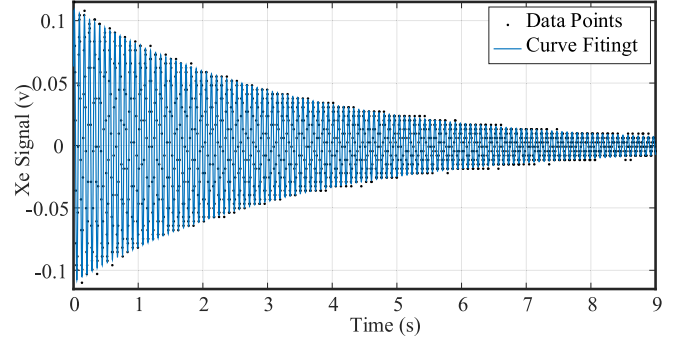


Fig. 14. Example of FID signal of ^{131}Xe isotope recorded from a sample PAXE01 (Pyrex coated with 10nm ALD Al_2O_3).

N_2 compared to CO are $50\times$, $6\times$, $0.5\times$, respectively, [43]. Absorbing other active gases faster than N_2 ensures a clean environment inside the cell.

It should be noted that this method of estimating the gas inside the cell has uncertainty associated with the spin destruction cross-section between Rb and other gases, which affect the broadening and frequency shift constants. The spin destruction cross-section used in our curve fitting was adopted from [38] and [39].

E. Experimental Setup

The atomic cell was placed in a miniaturized oven made from a thermally insulating material, all housed by a nested 4-layer μ -metal shield with integrated 3-axis magnetic field coils. The pump beam of 2.5mW with a circularly polarized light locked on Rb D1 line (795nm) along the z-axis. A DC field of $3.5\mu\text{T}$ and an RF field of 17.8kHz with an RMS amplitude of $3.5\mu\text{T}$ were applied along the z-axis. The probe beam was a linearly polarized beam of 1mW set off resonance from D2 line (780nm) and was applied along the y-axis. The produced RF signal was used as a reference for the lock-in amplifier that demodulated the output of the Faraday detector at the probe side (Faraday Detector is a balanced polarimeter used to detect Faraday Rotation). A $\pi/2$ pulse at the frequency of the Xe isotope of interest was applied along the y-axis to obtain the FID signal, which was fitted to an exponentially decaying sine wave to extract the relaxation time T_2 . Fig. 14 shows an example of the FID signal for ^{131}Xe of PAXE01.

F. Coating

Alkali metals, like Rb, react with glass cells at elevated temperatures, which leads to a consumption of the metal. One method to reduce this interaction is by passivating the glass walls of the cells. In [44], it was shown that a 20nm layer of Al_2O_3 can reduce the interaction between alkali metals and cell glass walls by $100\times$. It was also found that anodic bonding worked with ALD Al_2O_3 as an intermediate layer.

ALD is a thin film conformal coating technique, the reaction of two chemicals in a gas phase with a surface creates one atomic layer, for example, Trimethylaluminum (TMA) and H_2O creates Al_2O_3 . The process is self-limiting to a single atomic layer per cycle. The coating is achieved by repeating

TABLE III
SUMMARY OF ALD Al_2O_3 DEPOSITION PARAMETERS

	pulse time(s)	purge time(s)	N_{cycles}	N_2 rate [sccm]	Temp (°C)
TMA	0.015	10	100	20	200
H_2O	0.05	10	100	20	200

TABLE IV
SUMMARY OF CELLS USED IN THIS STUDY AND THE CORRESPONDING
RELAXATION TIMES OF EACH ISOTOPE

Cell	PXE01	PAXE01	HXE02
Glass	Pyrex	Pyrex	ASG
Coating	n/a	10nm Al_2O_3	n/a
^{129}Xe T_2 (s)	1.4	0.79	1.2
^{131}Xe T_2 (s)	0.74	3.55	2.35

deposition cycles until the desired thickness is reached. In our study, we used a commercial ALD deposition system by Cambridge Nanotech to deposit 10 nm of Al_2O_3 , on both samples and the capping wafer. The deposition parameters are summarized in Table III.

G. Results

Table IV summarizes the studied parameters and the average relaxation time of ^{129}Xe and ^{131}Xe isotopes in the range from 115°C to 140°C. We observed that Atomic Layer Deposition (ALD) of 10 nm Al_2O_3 on the cell walls increased the transverse relaxation time of the ^{131}Xe isotope by a factor of 3×, when compared to cells without coating. When using Aluminosilicate glass (ASG) instead of Borosilicate glass (Pyrex), we observed a similar effect on the relaxation time of ^{131}Xe isotope, demonstrating an increase of T_2 by a factor of 2.5×. On the other hand, ALD coating of Al_2O_3 was found to reduce the relaxation time of the ^{129}Xe isotope by a factor of 2×, while the ASG glass did not show a significant difference in T_2 of ^{129}Xe , as shown in Table IV.

H. Discussion

Reduction of the relaxation time of the ^{129}Xe isotope in PAXE01 (ALD Al_2O_3 coated cell) is believed to be due to a magnetic field gradient inside the cell created by non-uniform pumping of Rb atoms. This pumping non-uniformity is a result of different beam bending angles as it transmits through the cell, which was discussed earlier in section IV. Vertical pumping and in-plane probing of the same sample showed an increase of relaxation time to 1.22s, which is on par with PXE01, and that supports our hypothesis.

To analyze improvements of the relaxation time constant of ^{131}Xe , we performed Fast Fourier Transform (FFT) to the FID signal of ^{131}Xe of the three cells at temperature of 135°C. Subsequently, the FFT data were fitted with a triplet of Lorentzian functions. Table V summarizes the data fitting results. We observed two phenomena. The first observation is that the ALD Al_2O_3 coating and ASG glass suppressed quadrupole splitting by reducing the splitting frequency between the three peaks by 100× and 2.2×, respectively. The second observation is that ALD coating of Al_2O_3

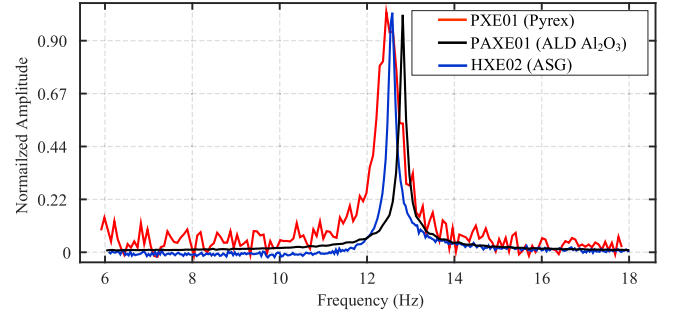


Fig. 15. FFT of the ^{131}Xe FID signal of PXE01(red), PAXE01(black), and HXE02(blue).

TABLE V
DATA FITTING RESULTS OF FFT OF THE ^{131}Xe FID SIGNAL TO TRIPLET
LORENTZIAN PEAKS FOR THREE CELLS

	Splitting (mHz)	Central Peak width (mHz)	Fitting RMSE
PXE01	153	509	4%
PAXE01	1.5	161	0.4%
HXE02	69.5	195	1.2%

and the use of ASG glass material reduced the width of the central peak by 3.2× and 2.5×, respectively. Fig. 15 shows FFT of FID signals of the three cells.

VI. CONCLUSION

We discussed different design considerations of micro-glassblown spherical cells for atomic sensors applications. These aspects included geometry, optical properties, material selection, and surface coating. We studied cell inner wall coating as well as cell glass materials. We found that 10nm ALD Al_2O_3 suppressed the quadrupole splitting of ^{131}Xe by 100× and reduced the central frequency peak width by 3×, which corresponds to a 3× increase in the relaxation time. We also found that using ASG glass instead of Pyrex suppressed the quadrupole splitting of ^{131}Xe by 2.2× and reduced the central frequency peak width by 2.5×, which corresponds to 2.5× increase in the relaxation time. We concluded that the ALD Al_2O_3 coating and the ASG glass did not have a significant impact on the T_2 of ^{129}Xe . In light of the experimental results and analytical models of NMRG ARW, [23], the NMRM fundamental sensitivity δB_n , [10], and assuming the same SNR values, the Al_2O_3 coating is projected to reduce the NMRG ARW and NMRM δB_n by more than threefold.

Although the scope and examples presented throughout the paper were focused on the atomic sensors applications, the design approach for producing highly spherical shells within the practical limits can be extended to other applications that utilize this fabrication technique. Examples of such applications include, but are not limited to, airflow [45], optical [21], [46], mechanical spherical resonators [47]–[49], and spherical shell gyroscopes [50].

ACKNOWLEDGMENT

Devices were designed, developed, and tested in Microsystems Laboratory, UC Irvine. The authors would like to thank UC Irvine INRF staff for their help with the fabrication, Dr. Larsen and Mr. Bulatowicz from Northrop Grumman Corp. for suggestions on improvement of the characterization setup, Danmeng Wang and Doreen Hii for their help in sample preparation, and Austin Parrish for his help with data fitting.

REFERENCES

- [1] R. M. Noor, N. Kulachenkov, M. H. Asadian, and A. M. Shkel, "Study on Mems glassblown cells for NMR sensors," in *Proc. IEEE Int. Symp. Inertial Sensors Syst.*, Naples, FL, USA, Apr. 2019, pp. 1–4.
- [2] S. Knappe, O. Alem, D. Sheng, and J. Kitching, "Microfabricated optically-pumped magnetometers for biomagnetic applications," in *Proc. J. Phys., Conf.*, vol. 723, 2016, Art. no. 012055.
- [3] R. Jiménez-Martínez and S. Knappe, "Microfabricated optically-pumped magnetometers," in *High Sensitivity Magnetometers*. Cham, Switzerland: Springer, 2017, pp. 523–551.
- [4] J. Kitching, E. A. Donley, E. Hodby, A. Shkel, and E. J. Eklund, "Compact atomic magnetometer and gyroscope based on a diverging laser beam," U.S. Patent 7872473 B2, Jan. 18, 2011.
- [5] S. A. Knappe, "Emerging topics: MEMS atomic clocks," in *Comprehensive Microsystems*, vol. 3, Amsterdam, The Netherlands: Elsevier, 2008.
- [6] L. M. Lust and D. W. Youngner, "Chip scale atomic gyroscope," U.S. Patent 7359059 B2, Apr. 15, 2008.
- [7] H. C. Abbink, E. Kanegsberg, and R. A. Patterson, "NMR gyroscope," U.S. Patent 7239135 B2, Jul. 3, 2007.
- [8] A. M. Shkel, "The chip-scale combinatorial atomic navigator," *GPS World*, vol. 24, no. 8, pp. 8–10, 2013.
- [9] M. Larsen and M. Bulatowicz, "Nuclear magnetic resonance gyroscope: For DARPA's micro-technology for positioning, navigation and timing program," in *Proc. IEEE Int. Freq. Control Symp.*, Laguna Beach, CA, USA, May 2012, pp. 1–5.
- [10] M. Bulatowicz and M. Larsen, "Compact atomic magnetometer for global navigation (NAV-CAM)," in *Proc. IEEE/ION Position, Location Navigat. Symp.*, Myrtle Beach, SC, USA, Apr. 2012, pp. 1088–1093.
- [11] Z. Wu, W. Happer, M. Kitano, and J. Daniels, "Experimental studies of wall interactions of adsorbed spin-polarized ^{131}Xe nuclei," *Phys. Rev. A, Gen. Phys.*, vol. 42, no. 5, pp. 2774–2784, 1990.
- [12] E. Donley, J. Long, T. Liebisch, E. Hodby, T. Fisher, and J. Kitching, "Nuclear quadrupole resonances in compact vapor cells: The crossover between the NMR and the nuclear quadrupole resonance interaction regimes," *Phys. Rev. A, Gen. Phys.*, vol. 79, no. 1, Jan. 2009, Art. no. 013420.
- [13] J. Kitching, "Chip-scale atomic devices," *Appl. Phys. Rev.*, vol. 5, no. 3, 2018, Art. no. 031302.
- [14] E. J. Eklund and A. M. Shkel, "Glass blowing on a wafer level," *J. Microelectromech. Syst.*, vol. 16, no. 2, pp. 232–239, Apr. 2007.
- [15] R. M. Noor, V. Gundeti, and A. M. Shkel, "A status on components development for folded micro NMR gyro," in *Proc. IEEE Int. Symp. Inertial Sensors Syst.*, Kauai, HI, USA, Mar. 2017, pp. 156–159.
- [16] R. M. Noor and A. M. Shkel, "MEMS components for NMR atomic sensors," *J. Microelectromech. Syst.*, vol. 27, no. 6, pp. 1148–1159, Dec. 2018.
- [17] M. H. Asadian, Y. Wang, R. M. Noor, and A. M. Shkel, "Design space exploration of hemi-toroidal fused quartz shell resonators," in *Proc. IEEE Int. Symp. Inertial Sensors Syst.*, Naples, FL, USA, Apr. 2019, pp. 1–4.
- [18] M. H. Asadian, Y. Wang, and A. M. Shkel, "Design and fabrication of 3D fused quartz shell resonators for broad range of frequencies and increased decay time," in *Proc. IEEE SENSORS*, New Delhi, India, Oct. 2018, pp. 1–4.
- [19] C. P. Martendal and A. P. N. de Oliveira, "Glass viscosity at crystallization temperature: An approach," *J. Therm. Anal. Calorimetry*, vol. 130, no. 3, pp. 1903–1912, Dec. 2017.
- [20] H. Wadell, "Volume, shape, and roundness of quartz particles," *J. Geol.*, vol. 43, no. 3, pp. 250–280, 1935.
- [21] C. Zhang, A. Cocking, E. Freeman, Z. Liu, and S. Tadigadapa, "On-chip glass microspherical shell whispering gallery mode resonators," *Sci. Rep.*, vol. 7, no. 1, Nov. 2017, Art. no. 014965.
- [22] J. T. Kajiya, "The rendering equation," *SIGGRAPH Comput. Graph.*, vol. 20, no. 4, pp. 143–150, Aug. 1986.
- [23] I. Greenwood and J. Simpson, "Fundamental noise limitations in magnetic resonance gyroscopes," in *Proc. Nat. Aerosp. Electron. Conf.*, Dayton, OH, USA, May 1977, pp. 1246–1250.
- [24] S. Schaefer, G. Cates, T.-R. Chien, D. Gonatas, W. Happer, and T. Walker, "Frequency shifts of the magnetic-resonance spectrum of mixtures of nuclear spin-polarized noble gases and vapors of spin-polarized alkali-metal atoms," *Phys. Rev. A, Gen. Phys.*, vol. 39, no. 11, p. 5613, 1989.
- [25] S. Appelt, A. B.-A. Baranga, C. Erickson, M. Romalis, A. Young, and W. Happer, "Theory of spin-exchange optical pumping of ^3He and ^{129}Xe ," *Phys. Rev. A, Gen. Phys.*, vol. 58, no. 2, p. 1412, 1998.
- [26] X. Liu, C. Chen, T. Qu, K. Yang, and H. Luo, "Transverse spin relaxation and diffusion-constant measurements of spin-polarized ^{129}Xe nuclei in the presence of a magnetic field gradient," *Sci. Rep.*, vol. 6, Apr. 2016, Art. no. 024122.
- [27] L.-A. Liew, S. Knappe, J. Moreland, H. Robinson, L. Hollberg, and J. Kitching, "Microfabricated alkali atom vapor cells," *Appl. Phys. Lett.*, vol. 84, no. 14, pp. 2694–2696, Jan. 2004.
- [28] E. J. Eklund, A. M. Shkel, S. Knappe, E. Donley, and J. Kitching, "Spherical rubidium vapor cells fabricated by micro glass blowing," in *Proc. IEEE 20th Int. Conf. Micro Electro Mech. Syst.*, Kobe, Japan, Jan. 2007, pp. 171–174.
- [29] E. J. Eklund, A. M. Shkel, S. Knappe, E. Donley, and J. Kitching, "Glass-blown spherical microcells for chip-scale atomic devices," *Sens. Actuators A, Phys.*, vol. 143, no. 1, pp. 175–180, 2008.
- [30] M. Hasegawa *et al.*, "Microfabrication of cesium vapor cells with buffer gas for MEMS atomic clocks," *Sensors Actuat. A, Phys.*, vol. 167, no. 2, pp. 594–601, 2011.
- [31] R. Lutwak *et al.*, "The chip-scale atomic clock-low-power physics package," Symmetricom-Technol. Realization Center, Beverly, MA, USA, Tech. Rep. ADA485257, 2004. [Online]. Available: <https://apps.dtic.mil/docs/citations/ADA485257>
- [32] M. Kwakernaak *et al.*, "Components for batch-fabricated chip-scale atomic clocks," Sarnoff Corp., Princeton, NJ, USA, Tech. Rep. ADA485258, 2004. [Online]. Available: <https://apps.dtic.mil/docs/citations/ADA485258>
- [33] S. Knappe *et al.*, "A microfabricated atomic clock," *Appl. Phys. Lett.*, vol. 85, no. 9, pp. 1460–1462, 2004.
- [34] Y. Pétremand *et al.*, "Microfabricated rubidium vapour cell with a thick glass core for small-scale atomic clock applications," *J. Microelectromech. Microeng.*, vol. 22, no. 2, 2012, Art. no. 025013.
- [35] A. Douahi *et al.*, "Vapour microcell for chip scale atomic frequency standard," *Electron. Lett.*, vol. 43, no. 5, pp. 33–34, Mar. 2007.
- [36] L. Nieradko *et al.*, "New approach of fabrication and dispensing of micromachined cesium vapor cell," *Proc. SPIE*, vol. 7, no. 3, 2008, Art. no. 033013.
- [37] P. Knapkiewicz, "Technological assessment of MEMS alkali vapor cells for atomic references," *Micromachines*, vol. 10, no. 1, p. 25, 2019.
- [38] M. D. Rotondaro and G. P. Perram, "Collisional broadening and shift of the rubidium D_1 and D_2 lines ($5^2\text{S}_{1/2} \rightarrow 5^2\text{P}_{1/2}, 5^2\text{P}_{3/2}$) by rare gases, H_2 , D_2 , N_2 , CH_4 and CF_4 ," *J. Quant. Spectrosc. Radiat. Transf.*, vol. 57, no. 4, pp. 497–507, 1997.
- [39] G. A. Pitz, A. J. Sandoval, T. B. Tafuya, W. L. Klennert, and D. A. Hostutler, "Pressure broadening and shift of the rubidium D_1 transition and potassium D_2 transitions by various gases with comparison to other alkali rates," *J. Quant. Spectrosc. Radiat. Transf.*, vol. 140, pp. 18–29, Jun. 2014.
- [40] G. Wertheim, M. Butler, K. West, and D. Buchanan, "Determination of the Gaussian and Lorentzian content of experimental line shapes," *Rev. Sci. Instrum.*, vol. 45, no. 11, p. 1369, 1974.
- [41] J. J. Olivero and R. Longbothum, "Empirical fits to the Voigt line width: A brief review," *J. Quant. Spectrosc. Radiat. Transf.*, vol. 17, no. 2, pp. 233–236, 1977.
- [42] *Si 101 Non-Evaporable Getters*, SAES Group, New Hartford, NY, USA, 2007.
- [43] S. Parkash and P. Vijendran, "Sorption of active gases by non-evaporable getter," *Vacuum*, vol. 33, no. 5, pp. 295–299, 1983.
- [44] S. Woetzel, F. Talkenberg, T. Scholtes, R. Ijsselstein, V. Schultze, and H.-G. Meyer, "Lifetime improvement of micro-fabricated alkali vapor cells by atomic layer deposited wall coatings," *Surf. Coat. Technol.*, vol. 221, pp. 158–162, Apr. 2013.
- [45] S. Liu, S. Pan, F. Xue, L. Nay, J. Miao, and L. K. Norford, "Optimization of hot-wire airflow sensors on an out-of-plane glass bubble for 2-D detection," *J. Microelectromech. Syst.*, vol. 24, no. 4, pp. 940–948, Aug. 2014.

- [46] E. Freeman, C.-Y. Wang, V. Sumaria, S. J. Schiff, Z. Liu, and S. Tadiadapa, "Chip-scale high Q-factor glassblown microspherical shells for magnetic sensing," *AIP Adv.*, vol. 8, no. 6, 2018, Art. no. 065214.
- [47] J. Giner and A. M. Shkel, "The concept of 'collapsed electrodes' for glassblown spherical resonators demonstrating 200:1 Aspect ratio gap definition," in *Proc. IEEE Int. Symp. Inertial Sensors Syst.*, Hapuna Beach, HI, USA, Mar. 2015, pp. 1–4.
- [48] J. Giner, J. M. Gray, J. Gertsch, V. M. Bright, and A. M. Shkel, "Design, fabrication, and characterization of a micromachined glass-blown spherical resonator with insitu integrated silicon electrodes and ALD tungsten interior coating," in *Proc. 28th IEEE Int. Conf. Micro Electro Mech. Syst.*, Estoril, Portugal, Jan. 2015, pp. 805–808.
- [49] I. P. Prikhodko, S. A. Zotov, A. A. Trusov, and A. M. Shkel, "Microscale glass-blown three-dimensional spherical shell resonators," *J. Micromech. Syst.*, vol. 20, no. 3, pp. 691–701, Jun. 2011.
- [50] S. A. Zotov, A. A. Trusov, and A. M. Shkel, "Three-dimensional spherical shell resonator gyroscope fabricated using wafer-scale glassblowing," *J. Microelectromech. Syst.*, vol. 21, no. 3, pp. 509–510, Jun. 2012.



Radwan M. Noor (S'17) received the B.Sc. degree in electrical engineering from King Abdulaziz University, Jeddah, Saudi Arabia, in 2008, the M.Sc. degree in electrical engineering from the University of Southern California, Los Angeles, CA, USA, in 2014, and the Ph.D. degree in electrical engineering and computer science with a focus on microelectromechanical systems (MEMS) from the University of California, Irvine, CA, USA, in 2019. He is currently an Assistant Research Professor with the National Center for MEMS technology, KACST,

Riyadh, Saudi Arabia. His research interests include design, modeling, and fabrication of solid-state and atomic MEMS inertial sensors.



Mohammad H. Asadian (S'15) received the B.S. and M.S. degrees in mechanical engineering from the Amirkabir University of Technology (Tehran Polytechnic), Tehran, Iran, in 2007 and 2010, respectively, and the M.S. and Ph.D. degrees in mechanical and aerospace engineering from the University of California, Irvine, CA, USA, in 2017 and 2019, respectively. His current interests include design, modeling, and control of MEMS inertial sensors and multi-sensor data fusion for navigation applications.



Andrei M. Shkel (F'99) received the diploma degree (Hons.) in mechanics and mathematics from Moscow State University, Moscow, Russia, in 1991, and the Ph.D. degree in mechanical engineering from the University of Wisconsin, Madison, WI, USA, in 1997. In 2000, he joined the Faculty Member with the University of California at Irvine, Irvine, CA, USA, where he is currently a Professor with the Department of Mechanical and Aerospace Engineering, with a joint appointment in the Department of Electrical Engineering and Computer Science, and the Department of Biomedical Engineering. He served as the Program Manager of Microsystems Technology Office, Defense Advanced Research Projects Agency (DARPA), Arlington, VA, USA, from 2009 to 2013. His professional interests are reflected in more than 250 publications. He holds more than 40 U.S. patents. His current research interests include center on the design, manufacturing, and advanced control of precision micromachined gyroscopes. He was a recipient of the 2002 George E. Brown, Jr. Award, the 2005 NSF CAREER Award, the 2006 UCI HSSoE Best Faculty Research Award, the 2009 IEEE Sensors Council Technical Achievement Award, and the UCI Samueli School of Engineering 2019 Innovator of the Year Award. In 2013, he was also a recipient of the Office of the Secretary of Defense Medal for Exceptional Public Service. He has served on a number of editorial boards, most recently, as an Editor of the IEEE/ASME JOURNAL OF MICROELECTROMECHANICAL SYSTEMS, an Editorial Board Member of the *Journal of Gyroscopy and Navigation*, and the Founding Chair of the IEEE International Symposium on Inertial Sensors and Systems. He was voted the 2018 President-Elect of the IEEE Sensors Council.